



Theoretical analysis and engineering application of controllable shock wave technology for enhancing coalbed methane in soft and low-permeability coal seams

Guodong Qiao^{1,2} · Zegong Liu^{1,2} · Yongmin Zhang³ · Changping Yi⁴ · Kui Gao¹ · Shigui Fu^{1,2} · Youzhi Zhao³

Received: 24 September 2023 / Revised: 26 November 2023 / Accepted: 29 February 2024
© The Author(s) 2024

Abstract

Coalbed methane (CBM) is a significant factor in triggering coal and gas outburst disaster, while also serving as a clean fuel. With the increasing depth of mining operations, coal seams that exhibit high levels of gas content and low permeability have become increasingly prevalent. While controllable shockwave (CSW) technology has proven effective in enhancing CBM in laboratory settings, there is a lack of reports on its field applications in soft and low-permeability coal seams. This study establishes the governing equations for stress waves induced by CSW. Laplace numerical inversion was employed to analyse the dynamic response of the coal seam during CSW antireflection. Additionally, quantitative calculations were performed for the crushed zone, fracture zone, and effective CSW influence range, which guided the selection of field test parameters. The results of the field test unveiled a substantial improvement in the gas permeability coefficient, the average rate of pure methane flowrate, and the mean gas flowrate within a 10 m radius of the antireflection borehole. These enhancements were notable, showing increases of 3 times, 13.72 times, and 11.48 times, respectively. Furthermore, the field test performed on the CSW antireflection gas extraction hole cluster demonstrated a noticeable improvement in CBM extraction. After antireflection, the maximum peak gas concentration and maximum peak pure methane flow reached 71.2% and 2.59 m³/min, respectively. These findings will offer valuable guidance for the application of CSW antireflection technology in soft and low-permeability coal seams.

Keywords CSW antireflection in coal seams · CBM extraction enhancement · Soft and low-permeability coal seams · Field test

1 Introduction

Coalbed methane (CBM) represents an unconventional natural gas. On the one hand, CBM has recently received worldwide attention because of its high calorific value and cleanliness (Busch and Gensterblum 2011; Liu et al. 2020; Qin et al. 2018; Sandoval et al. 2018). On the other hand, it is crucial to acknowledge that CBM also functions as a potent greenhouse gas, exerting an intensity of the greenhouse effect exceeding 20 times that of CO₂ (Tang et al. 2018). Moreover, CBM poses a significant risk of accidents in coal mines. Enhancing the efficiency of CBM extraction is of utmost importance in safeguarding both mine safety and environmental protection. As shallow coal mining reserves are depleted, Chinese coal mining has increasingly shifted to deeper depths at a rate of 10–25 m per year (Yuan 2016). Deeper coal seams are accompanied by elevated in-situ stress levels, resulting in low permeability and high gas

✉ Guodong Qiao
guodongqiao123@163.com

✉ Zegong Liu
zgliu@aust.edu.cn

¹ School of Safety Science and Engineering, Anhui University of Science and Technology, Huainan 232001, Anhui, China

² Institute of Energy, Hefei Comprehensive National Science Center, Hefei 230031, Anhui, China

³ School of Electrical Engineering, Xi'an Jiaotong University, Xi'an 710049, Shanxi, China

⁴ Division of Mining and Geotechnical Engineering, Luleå University of Technology, Luleå, Sweden

pressures (Meng et al. 2018; Si et al. 2019; Li et al. 2022). Deep coal seams exhibit a higher propensity for coal and gas outburst disasters in comparison to shallow coal seams (Tu et al. 2016), thereby presenting miners with an even greater safety threat. Techniques such as deep hole blasting, hydraulic fracturing, and CO₂ explosion have been employed to enhance coal seam permeability. (Xu et al. 2017; Yan et al. 2015; Wang et al. 2022; Zhu et al. 2023). However, these techniques are not effective when faced with soft and low-permeability coal seams. In view of this, the controllable shock wave (CSW) technology has been developed (Aici et al. 2012).

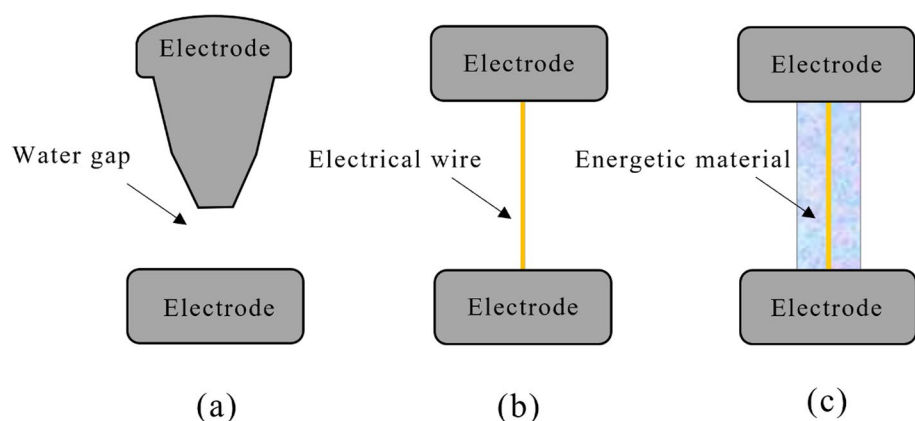
CSW technology is a type of high-voltage electrical pulse (HVP) technology (Cho et al. 2016). The discharge load is the core component that determines the strength of the shockwave pressure peak in HVP devices. Changing the type of discharge load has been found to enhance the magnitude of the peak shockwave pressure in CSW technology. Specifically, the conventional discharge load (water gap (WG)) in HVP can be replaced by electrical wires (EW) or energetic materials (EM) (Liu et al. 2017; Zhang et al. 2016; Zhou et al. 2015a). WG load suffers from low energy utilization and unstable discharge (Kristiansen et al. 1998), limiting its conversion to engineering applications. In contrast, the electrical wire explosion process influences the voltage on the wire, thereby reducing the pressure on the insulation structure and overcoming abnormal discharge faults in WG load (Grinenko et al. 2005). Electric wire explosion is a physical phenomenon where a substantial amount of electrical energy is deposited in the conductor before explosion. The stored electrical energy is rapidly released at the moment of explosion, causing a rapid phase change in the wire (Grinenko et al. 2005). The resulting plasma from the wire explosion expands rapidly, creating a shock wave in the surrounding water medium. Furthermore, the energy conversion efficiency of EW load has improved by approximately 24%, overcoming the problem of energy leakage from WG load (Zhou et al. 2015a). However, the energy generated by

the EW load is insufficient for application at antireflective coal seam engineering sites. To further enhance the peak pressure of the shockwave, researchers developed the EM load. A schematic of the three discharge load types is shown in Fig. 1.

The EM load was a hybrid structure containing metal wires (core), EM (mantle), and plastic tubes (shell) (Liu et al. 2017). Several formulations were used to identify high-performance EM loads. Examples include aluminium-containing mixtures (Zhou et al. 2015b); a mixture of ammonium nitrate and ammonium perchlorate (Han et al. 2015); and a mixture of nitromethane and copper oxide powder (Hu et al. 2022). The chemical explosion of the EM depends on the physical explosion of the EW. Specifically, the plasma generated after the EW explosion is the key to igniting the EM. The ignition mechanism of EM is similar to that of plasma ignition in electrothermal-chemical guns (Taylor 2002). EM combines the advantages of EW (controllability and fast frontier) with those of explosives (long duration and high energy) (Han et al. 2015). CSW-fractured coal seams have reached a size suitable for engineering applications due to the successful application of EM discharge loads (Lin and Zhang 2022).

In addition to the discharge load of the CSW, the response of coal porosity and fracturing to the action of CSW was also investigated. Extensive indoor experiments were conducted before the field tests, and the results provided data supporting the use of CSW for enhanced CBM extraction. (Shi et al. 2016) conducted a study to investigate the influence of varying impact numbers and shockwave intensities on coal permeability. The response of immeasurable pores (< 3 nm) in the coal body was found to be more pronounced than that of other types of pores in the CSW technique, and significant variations were observed in the response of immeasurable pores to CSW, attributed to the differing mechanical strengths of coal types. Furthermore, high-energy shocks expedite the evolution of pore space. To

Fig. 1 Discharge loads of EHD:
a WG b EW c EM



further investigate the effect of shock wave energy on coal fractures (Zhou et al. 2015b), used shock waves with different energies to impact the coal samples. Significant differences in the distribution density of fractures were observed among samples following the application of shock waves with varying energies. Higher energy shock waves resulted in extensive fracturing of the coal body. (Li et al. 2021) found that the fractal dimension of the sample is positively correlated with the number of impacts, regardless of the degree of coal metamorphism. The cracks and permeability in the coal-rock combination exhibited a similar response to CSW, consistent with the findings of the aforementioned study (Zhao 2021). In conclusion, the results of these experiments show that the pore structure within coal can be effectively modified using CSW technology, thus increasing the permeability of coal. These changes in coal are beneficial for increasing CBM production.

Soft and low-permeability coal seams are widely acknowledged to exhibit a higher susceptibility to the occurrences of coal and gas outburst disasters. However, there are currently more reported indoor experiments using CSW technology to enhance CBM extraction while field trials on soft and low-permeability coal seams have not yet been reported. Currently, mathematical models for describing the CSW technology to fracture coal seams are not available. In the present paper, a mathematical model was proposed to describe the CSW antireflection coal seams. The radius of the effective range of influence for the CSW, calculated using the mathematical model, was used to design the field test protocol. Finally, field trials were conducted using CSW technology to enhance CBM extraction, and the availability and effectiveness of CSW technology for CBM production enhancement were evaluated. The findings of the study will offer valuable guidance

for the widespread adoption of CSW technology in coal mines that encounter soft and low-permeability seams.

2 Theoretical analysis of CSW antireflection coal seam

2.1 CSW antireflective coal seams profile

Based on the above research, CSW devices have been recently developed and received considerable attention. Figure 2 illustrates the composition of the CSW equipment. It comprises a pulsed power control device, magnetic positioner, high-voltage power supply, pulsed capacitor, energy controller, shockwave generator, and EM pusher. Please note that the EM discharge load was installed in the shockwave generator before the operation of the equipment. After the EM was detonated, an EM pusher pushed a new EM discharge load into the shockwave generator. This design ensures continuous operation of the CSW without withdrawing the device from the borehole. Contrary to conventional EHD equipment in the laboratory, the rest of the CSW, except for the pulse power control unit, is integrated into a rigid cylinder to be suitable for coal seam permeability enhancement. This rigid cylinder is called an in-hole unit, and the pulse power control unit is called an out-hole unit.

The borehole was filled with water during the CSW penetration of the coal seams. Compared with hydraulic fracturing, CSW antireflection technology uses very little water and is suitable in water-stressed mining areas. In addition, water and air have different physical and mechanical properties. In general, water can hardly be compressed. However, it becomes compressible when subjected to high pressures such as an explosion. Simultaneously, the internal energy increment on the shock wave front in water is twice that in

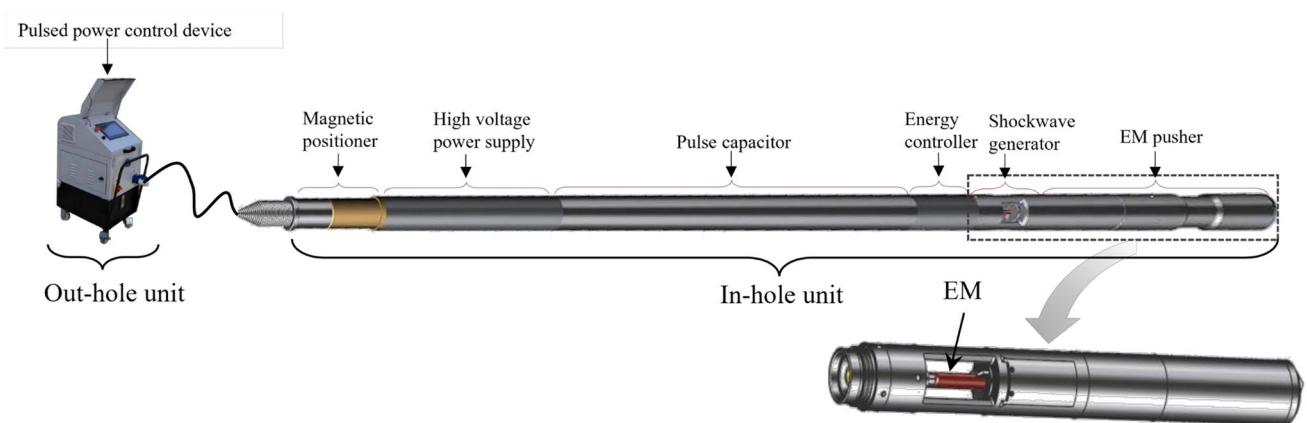


Fig. 2 Components of CSW equipment

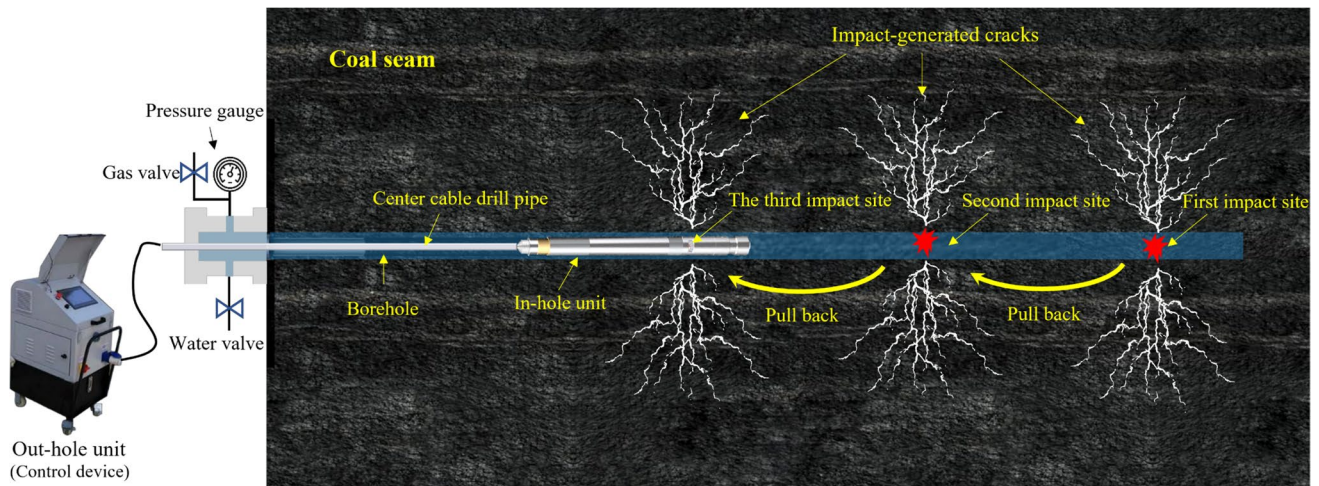


Fig. 3 CSW multi-point repetitive impact coal seam schematic

air (Yuwen 2006), which implies a higher energy utilisation of the CSW. In summary, CSW is considered environmentally friendly, safe, and efficient. Figure 3 demonstrates the CSW fracturing process of the coal seam.

During CSW, the EM is detonated in water, producing a high-temperature and high-pressure burst product that expands outward rapidly. The aqueous medium undergoes strong compression, resulting in a shockwave propagating away from the source of the explosion. The wavefront of the shockwave is steep and travels faster than sound. Despite its initial high energy, the shockwave quickly dissipates, leading to a relatively small affected area. A crushed zone is formed by the compressive-shear damage of the shock wave. As the distance from the center of the explosion increases, the shockwave transitions into an elastic wave. The application of stress waves induces a stretching mechanism that leads to plastic deformation within the coal seam, consequently giving rise to the development of a fracture zone. The stress wave eventually decays into an elastic wave. As elastic waves possess lower energy, the coal seam exhibits elastic deformation rather than plastic deformation under its influence. The elastic wave has the widest range of effect, primarily affecting the vibration zone. The attenuation pattern of the stress wave and its range influence are depicted in Fig. 4.

The generation of particulate matter within the crushed region consumes a significant portion of the explosive energy (Lu et al. 2016). Therefore, the size of the crushed zone impacts the conversion efficiency of CSW energy. The dimensions of the fracture zone directly impact the extent of permeability enhancement in the coal seam, acting as a conduit for gas transportation. In the case of soft coal seams with low hardness, excessive impact loads can lead to coal crushing, thereby impeding gas extraction.

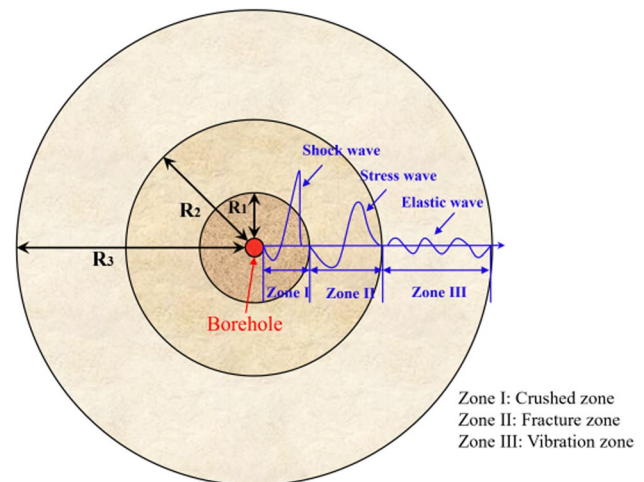


Fig. 4 CSW influence range and stress wave attenuation

Hence, it is imperative to develop a mathematical model that defines the extent of the crushed and fracture zones. Such a model would greatly facilitate future investigations into CSW antireflection in coal seams.

2.2 Mathematical model of CSW fracturing and crushed range

2.2.1 Dynamic response of coal seam under CSW loading

The pressure generated by CSW loading on the borehole wall was calculated based on explosive blasting theory. This is because CSW uses a HVP to drive the wire to explode, igniting the EM (Hu et al. 2022; Liu et al. 2019; Shi et al. 2021), which can be analogous to using a detonator to ignite

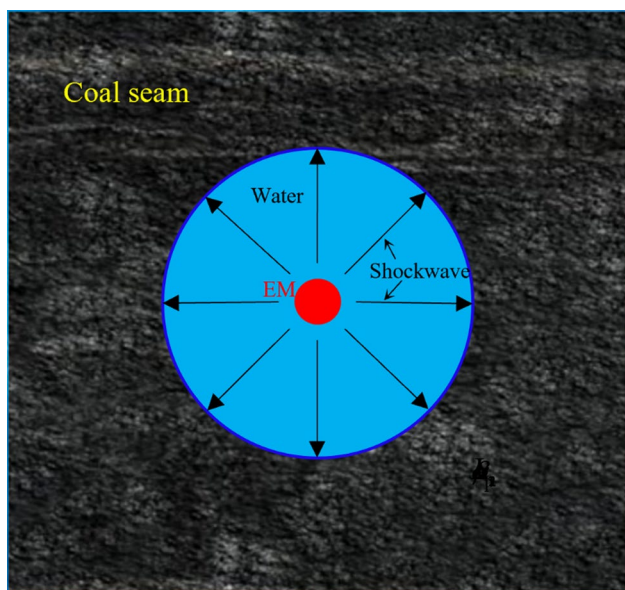


Fig. 5 Diagram of anti-reflection hole wall loaded by CSW

explosives. Moreover, the waveform characteristics caused by the CSW are similar to those of a blast shock wave (Li 2015). Figure 5 shows the borehole wall is loaded after the EM is detonated in water.

In the analysis of the dynamic stress field of blasting, a number of functions describing the decay of the blast loading with time have been developed. Earlier load functions ignored the rise time of the blast load (Sharpe 1942). However, Cho’s (Cho et al. 2003) study as well as Ma’s (Ma and An 2008) both demonstrated the significant influence of rise time on the crushed and fracture zones. Trivino’s load function addresses this issue by defining both the rise and fall times of the blast load (Trivino et al. 2009). However, Trivino’s equation is complicated due to the variation of Laplace and the inversion of the analytical solution. On the other hand, Duvall’s model (Duvall 1953) incorporates the rise time of the blast load and is easily utilized with the Laplace transform. The specific form of Duvall’s model is presented as Eq. (1):

$$P(t) = P_0[e^{-\alpha t} - e^{-\beta t}] \tag{1}$$

where P_0 denotes pressure, α and β are constants. According to laboratory data, the peak pressure on the blast hole wall caused by the EM explosion is $P_{\max} = 222.43$ MPa. Figure 6 portrays the temporal pattern of CSW-induced pressure on the borehole wall, as determined through experimental measurements, along with the corresponding curve fitted to the observed data. The equation representing the fitted curve is as follows:

$$P(t) = 1349.78[e^{-93330.68t} - e^{-126770.22t}] \tag{2}$$

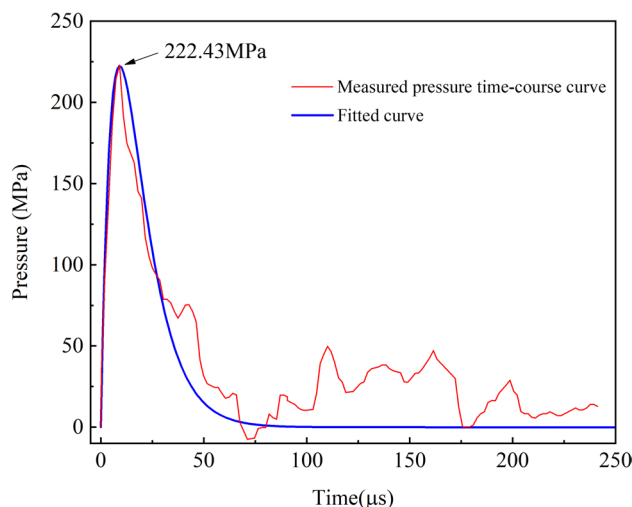


Fig. 6 The blast load curve

2.2.2 Theoretical analysis

Assuming the anti-reflection borehole wall is subjected to a uniform blast load pressure following EM blasting, and considering the coal as a homogeneous, elastic, and isotropic material, the CSW antireflection coal seam can be regarded as a linear elastic plane strain problem. Consequently, the governing equations for elastic waves in coal seams, which encompass initial and boundary conditions, can be expressed in column coordinates (Miklowitz 1978):

$$\begin{cases} \frac{\partial^2 \varphi(r,t)}{\partial r^2} + \frac{1}{r} \frac{\partial \varphi(r,t)}{\partial r} = \frac{\partial^2 \varphi(r,t)}{C_p^2 \partial t^2} & (r > a, t > 0) \\ \varphi(r, 0) = \dot{\varphi}(r, 0) = 0 & (r \geq a) \\ \lim_{r \rightarrow \infty} \varphi(r, t) = 0 & (t > 0) \\ \sigma_r(a, t) = p(t) \end{cases} \tag{3}$$

where $\varphi(r, t)$ represents the displacement potential function, r denotes the radii, and t represents time. C_p corresponds to the longitudinal wave velocity, σ_r signifies the radial stress and $p(t)$ denotes the load exerted on the wall of the anti-reflection borehole. Equation (3) cannot get a general solution, so a Laplace transform in the form of Eq. (4) is carried out:

$$\frac{\partial^2 \bar{\varphi}}{\partial r^2} + \frac{1}{r} \frac{\partial \bar{\varphi}}{\partial r} - k_d^2 \bar{\varphi} = 0 \tag{4}$$

where $\bar{\varphi}$ is the Laplace transform of $\varphi(r, t)$, $k_d = s/C_p$ and s is the parameter related to the Laplace transform. The general solution of Eq. (4) can be expressed as Eq. (5):

$$\bar{\varphi}(r, s) = A(s)I_0(k_d r) + B(s)K_0(k_d r) \tag{5}$$

where I_0 and K_0 are the first and second kind of the 0th-order modified Bessel function, respectively.

The relationship between the displacement $u(r, t)$ and the displacement potential function $\varphi(r, t)$ is

$$u(r, t) = \frac{\partial \varphi(r, t)}{\partial r} \tag{6}$$

Further, the stress and the displacement potential functions satisfy Eq. (7):

$$\begin{cases} \sigma_r(r, t) = \lambda \nabla^2 \varphi + 2\mu \frac{\partial^2 \varphi}{\partial r^2} \\ \sigma_\theta(r, t) = \lambda \nabla^2 \varphi + (2\mu/r) \frac{\partial \varphi}{\partial r} \\ \sigma_z(r, t) = \nu(\sigma_r + \sigma_\theta) \end{cases} \tag{7}$$

where ν denotes Poisson’s ratio. λ and μ are Lamé constants, which can be found from ν and Young’s modulus E . Specifically, $\lambda = \nu E / [(1 + \nu)(1 - 2\nu)]$, $\mu = E / (2\nu + 2)$.

The Laplace transform of σ_r is

$$\bar{\sigma}_r(r, t) = \lambda \nabla^2 \bar{\varphi} + 2\mu \frac{\partial^2 \bar{\varphi}}{\partial r^2} = (\lambda + 2\mu) \frac{\partial^2 \bar{\varphi}}{\partial r^2} + \frac{\lambda}{r} \frac{\partial \bar{\varphi}}{\partial r} \tag{8}$$

By combining Eq. (6) and Eq. (8) and utilizing the recurrence relations of the Bessel function, Eq. (9) can be obtained:

$$\bar{\sigma}_r(r, t) = \left[(\lambda + 2\mu)k_d^2 K_0(k_d r) + 2\mu k_d K_1(k_d r)/r \right] B(s) \tag{9}$$

Carrying out the Laplace transform for the boundary condition of $\sigma_r(a, t) = p(t)$, Eq. (9) can be got:

$$\bar{\sigma}_r(a, s) = \bar{P}(s) \tag{10}$$

Combining Eqs. (9) and (10), Eq. (11) can be got:

$$B(s) = \frac{\bar{P}(s)}{(\lambda + 2\mu)F(s)} \tag{11}$$

Since Eq. (3) cannot be solved directly, it is processed with Laplace transform. The displacement potential functions, stresses, and displacements can be obtained:

$$\begin{cases} \bar{\varphi}(r, s) = \frac{\bar{P}(s)K_0(k_d r)}{(\lambda + 2\mu)F(s)} \\ \bar{\sigma}_r(r, s) = \frac{(2/D^2 r)K_1(k_d r) + k_d K_0(k_d r)}{(2/D^2 a)K_1(k_d a) + k_d K_0(k_d a)} \bar{P}(s) \\ \bar{\sigma}_\theta(r, s) = \frac{(-2/D^2 r)K_1(k_d r) + (1 - 2/D^2)k_d K_0(k_d r)}{(2/D^2 a)K_1(k_d a) + k_d K_0(k_d a)} \bar{P}(s) \\ \bar{u}(r, t) = \frac{\partial \bar{\varphi}(r, t)}{\partial r} = -\frac{\bar{P}(s)k_d K_1(k_d r)}{(\lambda + 2\mu)F(s)} \end{cases} \tag{12}$$

where $D^2 = (\lambda + 2\mu) / \mu$, $F(s) = (2k_d / D^2 a)K_1(k_d a)$ $F(s) = (2k_d / D^2 a)K_1(k_d a) + k_d^2 K_0(k_d a)$. K_0 and K_1 represent the modified Bessel functions of the second kind, corresponding to the 0th and 1st orders, respectively. The above expression does not allow for the analytical inversion of the Laplace transform. Nevertheless, there exist several methods for numerically inverting the Laplace transform (Cohen 2007; Dubner and Abate 1968; Durbin 1974). Dubner’s method is used in this paper (Dubner and Abate 1968).

To explore the dynamic response of coal in the study of the CSW antireflection coal seam, the load curve depicted in Fig. 6 is applied to the antireflection hole wall. In this paper, the diameter of the borehole for the CSW antireflection is 127 mm, and the P-wave velocity in the coal seam is $C_p = 1539$ m/s, and the S-wave velocity is $C_s = 1088$ m/s. The numerical inversion results of the Laplace transform are presented in Fig. 7. Specifically, Fig. 7a displays the radial stress time-course curve at various blasting center distances. The curves reveal that the maximum peak stress in the radial direction is compressive and decreases rapidly as the blasting center distance increases. Conversely, Fig. 7b illustrates the hoop stress results, with the maximum peak stress being tensile. These findings align with previous studies (Rossmannith et al. 1997).

2.2.3 Calculation of the extent of the crushed and fracture zones

The failure criterion of a material under blast loading is dependent on the material’s nature and the actual stress conditions (Sun 1987). Coal, being a brittle material, exhibits significantly lower tensile strength compared to its compressive strength. In engineering blasting scenarios, coal experiences a three-way stress state consisting of mixed tensile and compressive stresses. Within the crushed zone, the primary mode of damage is caused by the shock wave compression, resulting in particle cracking and microcracking (Esen et al. 2003). In the fracture zone, the medium primarily undergoes radial compression due to the stress wave, leading to shear tensile stresses. The shear tensile component of the stress wave serves as the primary controlling factor for the generation of radial fractures within the fracture zone (Xie et al. 2017). Under plane strain conditions, the stress intensity at any point in the coal can be represented by the following equation:

$$\sigma_i = \frac{1}{\sqrt{2}} \left[(\sigma_r - \sigma_\theta)^2 + (\sigma_\theta - \sigma_z)^2 + (\sigma_z - \sigma_r)^2 \right]^{\frac{1}{2}} \tag{13}$$

where σ_r , σ_θ and σ_z are radial, hoop and shear stresses, respectively.

According to the Mises criterion, coal is damaged when σ_i satisfies the following conditions (Dai 2001):

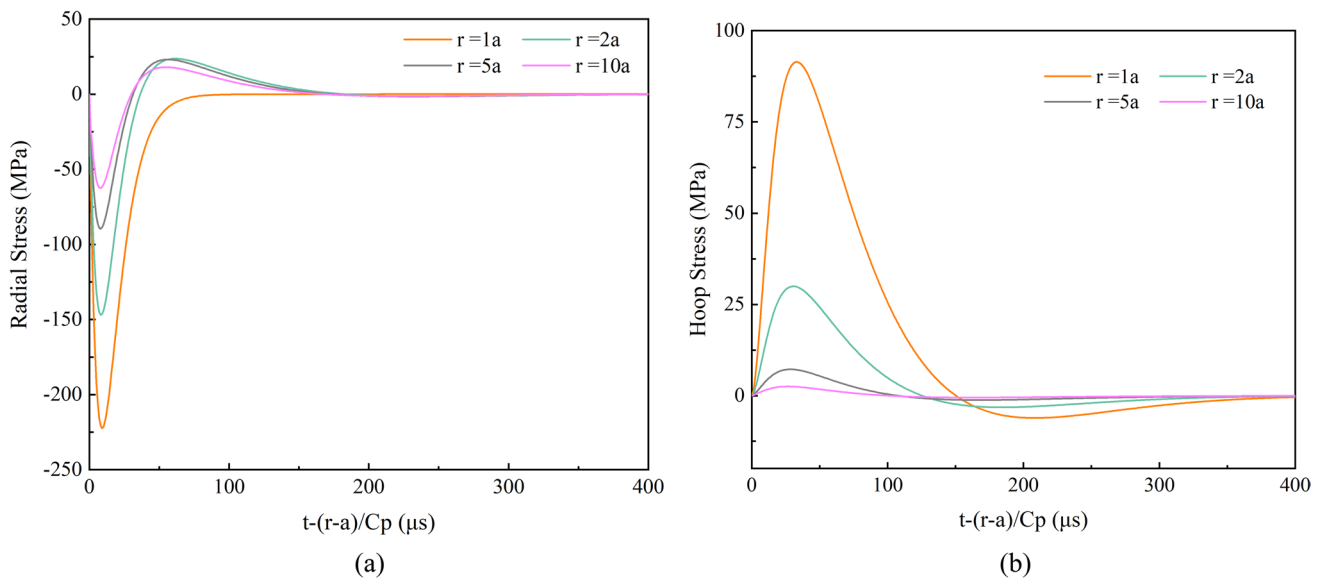


Fig. 7 Radial and hoop stresses from Laplace transform inversions **a** Radial stress time course curve **b** Hoop stress time course curve

$$\sigma_i \geq \sigma_0 \tag{14}$$

$$\sigma_0 = \begin{cases} \sigma_{cd} \text{ (crushing zone)} \\ \sigma_{td} \text{ (fracture zone)} \end{cases} \tag{15}$$

Further, the stress conditions of the coal on the boundaries of the crushed and fracture zones follow Eq. (16) (Fan et al. 2022):

$$\begin{cases} \sigma_r = \sigma_{cd} \text{ (crushing zone)} \\ \sigma_\theta = \sigma_{td} \text{ (fracture zone)} \end{cases} \tag{16}$$

where σ_{cd} and σ_{td} denote uniaxial dynamic compressive strength and uniaxial dynamic tensile strength, respectively.

The dynamic compressive strength $\sigma_{cd} = \sigma_c \dot{\epsilon}^{\frac{1}{3}}$, where σ_c and $\dot{\epsilon}$ are the static compressive strength and strain rate, respectively. Specifically, $\dot{\epsilon} = 10^2 \sim 10^4 \text{ s}^{-1}$ (Dai 2001). Under water-coupled borehole blasting conditions, $\dot{\epsilon}$ is generally taken to be equal to 10^3 s^{-1} (Zong et al. 2012). The dynamic tensile strength σ_{td} is equal to the static tensile strength σ_t over the range of strain rates for rock blasting (Wang 1984). In this paper, $\sigma_c = 7.7 \text{ MPa}$ and $\sigma_t = 0.75 \text{ MPa}$. Thus Eq. (16) can be written as:

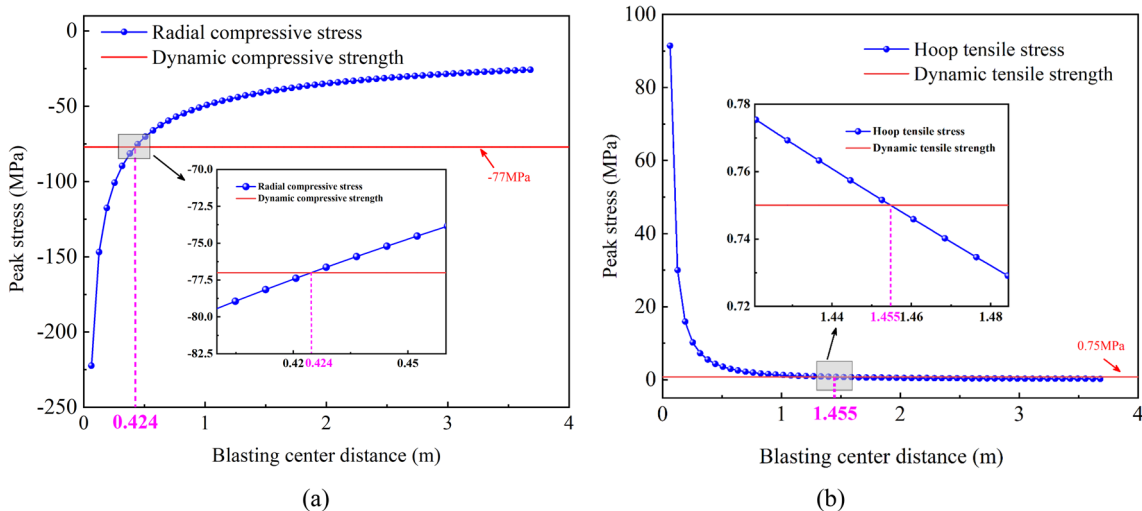


Fig. 8 Attenuation curve of peak stresses **a** Radial peak stress **b** Hoop peak stress

$$\begin{cases} \sigma_r = \sigma_{cd} = 77 \text{ MPa (crushing zone)} \\ \sigma_\theta = \sigma_{td} = 0.75 \text{ MPa (fracture zone)} \end{cases} \quad (17)$$

Figure 8 illustrates the decay curves of radial and hoop peak stresses with increasing distance from the blasting center. Based on Eq. (17), the crushed and fracture zones have radii of $R_1 = 42.4$ cm and $R_2 = 1.455$ m, respectively, when subjected to CSW.

2.3 Mathematical model of effective CSW influence range

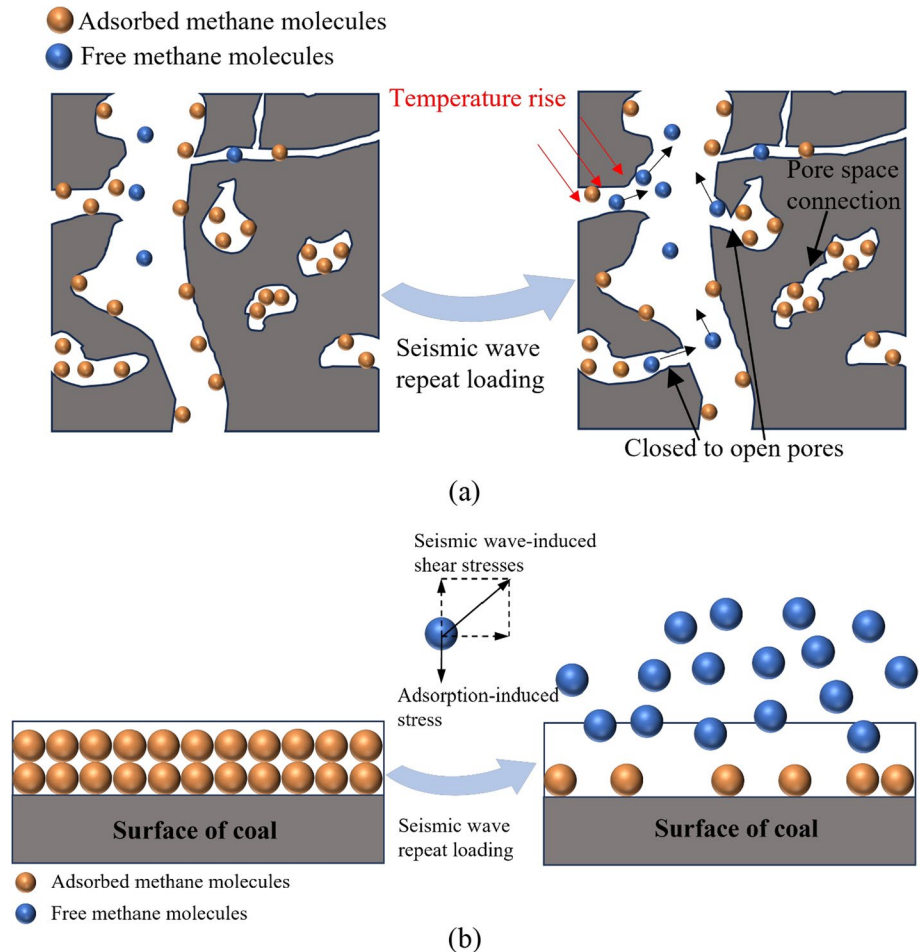
2.3.1 Definition of effective CSW influence range

Deep-hole blasting is commonly employed to fracture coal seams, typically using a single-shot approach. In this method, the contribution of seismic waves to coal seam permeability is minimal compared to that of shock waves and stress waves. Consequently, the impact of seismic waves on coal is often disregarded. However, when employing CSW technology to enhance coal seam permeability, the coal

seams are subjected to multiple seismic wave loadings. Consequently, it becomes essential to re-evaluate the effects of seismic waves on coal. Previous experimental studies have demonstrated that repeated impacts of CSW on coal samples effectively enhance the microscopic pore space within coal seams (Shi et al. 2016). Under the repeated loading of seismic waves, the microscopic pores in coal undergo fatigue fracture, leading to the modification of closed micropores into open pores (Li 2015), as depicted in Fig. 9a.

The repeated loading of seismic waves can enhance methane desorption from coal. A seismic wave is a stress wave that induces sliding friction at crack surfaces and grain boundaries within a medium. A portion of the seismic wave's energy is utilized to overcome friction and is converted into thermal energy (Johnston et al. 1979). Moreover, when the compression wave traverses the coal seam, non-uniform compression leads to the formation of a non-uniform temperature field. Heat conduction occurs between these temperature fields, resulting in the conversion of fluctuating energy into thermal energy through an irreversible process (Jackson and Anderson 1970). This

Fig. 9 Gas desorption under repetitive loading of seismic waves **a** Changes in pore structure and gas desorption **b** Seismic waves strip methane molecules from coal surfaces



phenomenon is amplified by the repetitive effects of seismic waves. The higher the temperature within the coal, the easier it becomes for methane molecules to escape from Van der Waals forces, leading to an increase in the number of free methane molecules (Wu et al. 2016). Figure 9a illustrates the desorption of adsorbed methane molecules into free methane molecules due to temperature elevation. Furthermore, the repeated loading of seismic waves strips methane molecules from the coal surface (Sun et al. 2015), as depicted in Fig. 9b. It further augments the quantity of free methane molecules, thereby facilitating the extraction of CBM. Consequently, the region where the CBM extraction was enhanced under the influence of the CSW was identified as the effective CSW influence range. The vibration velocity of coal at the boundary of the effective CSW influence range is greater than zero. As the energy of the seismic wave attenuates during its propagation to the boundary in the vibration zone, it no longer possesses sufficient energy to induce vibration in the coal. Consequently, the coal at the boundary of the vibration zone comes to a state of rest. The effective boundary of the CSW influence range is evidently confined within the broader expanse of the vibration zone.

2.3.2 Calculation of the effective CSW influence range

The peak particle vibration velocity (PPV) is introduced to define the effective CSW influence range. EM explosions produce a cylindrical wave, and the effect of the decay of the PPV of the coal mass is given (Hustrulid and Lu 2002)

$$V = kV_0 \left(\frac{a}{r} \right)^\eta \quad (18)$$

where k is a parameter related to the number of blast holes. For the CSW technique, each stage of the shock wave is caused by an EM discharge load. Therefore, $k = 1$. η is the vibration velocity decay exponent, which can be expressed as follows:

$$\eta = \kappa + \xi \quad (19)$$

κ and ξ are the geometric and damping attenuation indices of column surface waves, respectively. The literature (Jin 2013) states that $\kappa = 0.5$. The value of ξ depends on the propagation medium of the seismic wave and can be expressed as follows:

$$\xi = \alpha - \gamma \quad (20)$$

Coal is a typical soft rock with $\alpha = 1.8$ (Regulation 2014) and γ is the geometric decay indices of the concentrated charge package, where $\gamma = 1$ (Shao 2014).

V_0 is the PPV at the borehole wall. V_0 is expressed as follows:

$$V_0 = \frac{P_{\max}}{\rho_2 C_{p2}} \quad (21)$$

Radius R_3 of the effective CSW influence range can be obtained:

$$R_3 = r = a \left(\frac{kP_{\max}}{V\rho C_p} \right)^{1/(\kappa+\alpha-\gamma)} \quad (22)$$

where ρ is the density of coal, which in this paper is 1440 kg/m³.

PPV of brittle materials, such as rocks that produce tiny cracks, is 25 cm/s (Bauer and Calder 1978). The surface of the coal repeatedly loaded with seismic waves generated by the CSW may not exhibit visible cracks. CBM extraction from coal seams whose micropores were altered by CSW was enhanced. Based on previous in-laboratory experience, the PPV of coal at the edge of the effective CSW influence range was temporarily assigned at 12.5 cm/s in this study. The effective CSW influence range can be derived:

$$\begin{aligned} R_3 &= r_b \left(\frac{kP_{\max}}{V\rho_2 C_{p2}} \right)^{1/(\kappa+\alpha-\gamma)} \\ &= 0.0635 \text{ m} \\ &\quad \times \left(\frac{1 \times 222.43 \text{ MPa}}{12.5 \text{ cm/s} \times 1440 \text{ kg/m} \times 1539 \text{ m/s}} \right)^{1/1.3} \\ &= 10.29 \text{ m} \end{aligned} \quad (23)$$

3 Field test of CSW permeability enhancement

3.1 Test site description

The Xieqiao coal mine belongs to Huaihe Energy (Group) Co. It is situated in the southwestern part of the Huabei Plain in Anhui Province, China, as depicted in Fig. 10. The well field is approximately 20 km in the east–west direction, with an inclination width of 2.9–4.3 km and an area of approximately 38.20 km². The Xieqiao well field is a fully concealed coal-bearing area, and the strata drilled include Cambrian, Ordovician, Carboniferous, Permian, Triassic, and Cenozoic in order from old to new, with the thickness of Cenozoic strata ranging from 194.1 to 485.64 m, averaging 363.26 m. The mine's mean absolute and mean relative gas emission rates were 202.39 m³/min and 12.31 m³/t, respectively, thus it is identified as a gas outburst mine. Due to the C13-1 coal seam's low permeability, extracting CBM poses significant challenges. The application of various antireflection techniques in the past has proven to be ineffective.

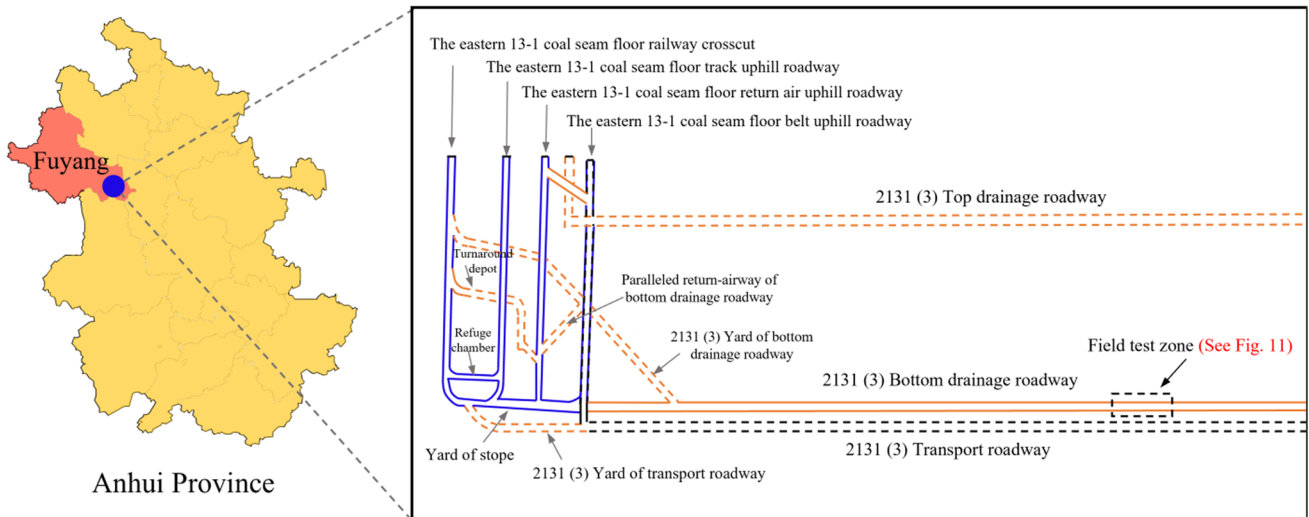


Fig. 10 Location of CSW technology test area

The 2131 (3) bottom drainage roadway was chosen as the test area to validate the effectiveness of CSW technology for enhanced CBM extraction, as shown in Fig. 10. The C13-1 seam showed stability as a target seam with thicknesses ranging from 0.2 to 8.1 m and an average thickness of 5.9 m. Elevation measurements of the seam range from – 810 to – 894 m. Adjacent to the target coal seam, there is the C13-2 seam located in the roof, approximately 3.7 m away, averaging at 0.5 m. Furthermore, within 3.3 m from the target seam, there is the C12 seam situated in the floor.

3.2 Patterns of layout of holes and test processes

Drilling sites 29# and 30# were selected as the field test zone in this trial. To assess the impact of CSW anti-reflection on single-hole gas extraction, a field trial was conducted at the 30# drilling site. Similarly, the field trial to evaluate the influence of CSW antireflection on the extraction of borehole clusters was performed at drilling site 29#. Figure 11 depicts a diagram illustrating the CSW antireflection coal seam.

Fig. 11 Schematic of the field test profile

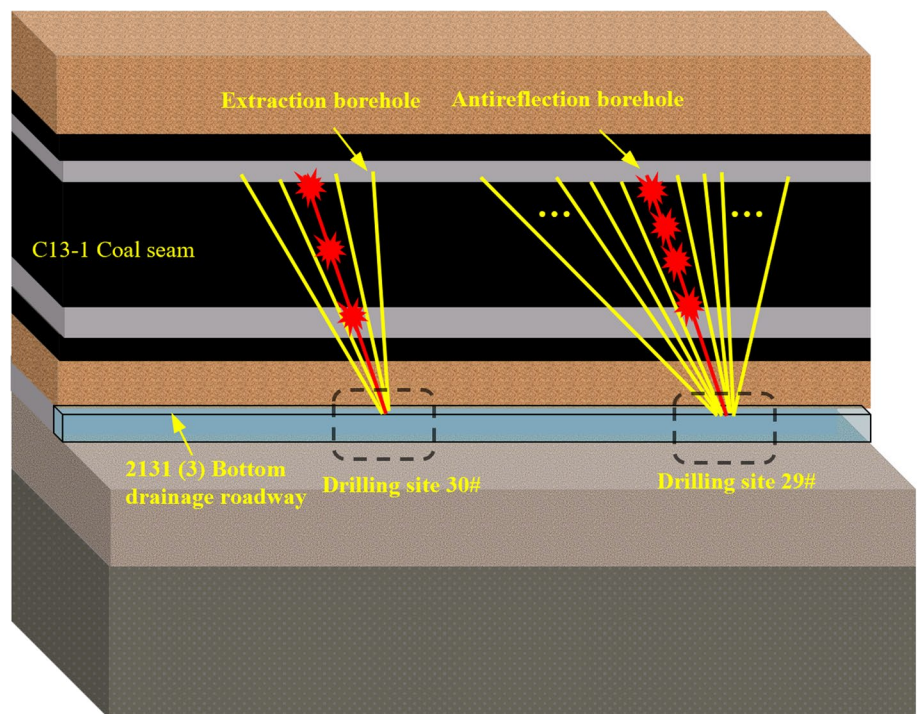


Table 1 Design parameters of the borehole in drilling site 30#

Borehole	Diameter of hole (mm)	Azimuth (°)	Dip angle (°)	Hole depth (m)
C1	127	184.1	26.2	56
K1	94	191	33.8	35
K2	94	173.9	32.6	36
K3	113	197.9	26.2	43
K4	113	164.6	23.9	47

The theoretical value of the CSW effective influence radius is a guide to setting the distance between the inspection hole and the antireflection borehole. Specifically, if the distance between the holes is too large, the inspection holes will not be affected by the CSW, while if the distance between the holes is too small, the effective range of influence of the CSW will not be verified. Five boreholes were drilled in the drilling site 30#, including an antireflection hole (C1), two gas pressure measurement holes (K1 and K2), and two inspection holes (K3 and K4). Table 1 presents the detailed design parameters for all boreholes.

K1 and K2 were employed to monitor the variation in coal seam gas pressure prior to and subsequent to the enhancement of seam permeability. Thus, the change in the coal seam permeability was calculated. These must be set within the influence of an antireflection hole. According to

Sect. 2.3.2, $R_3 = 10.29$ m. Thus, the distances between K1, K2, and C1 were set as 5 m (less than 10.29 m). K3 and K4 were utilized to assess the alterations in gas extraction before and after an augmentation in coal seam penetration. The distance between K3 and C1 was set to 10 m. The distance between K4 and C1 was set to 15 m. Figure 12a illustrates the opening position of the borehole. Figure 12b provides a top view of the test area. Figure 12c displays a section of the drilling site 30# and depicts the spatial relationship between the borehole and coal seam.

3.3 Variation of gas permeability coefficient of the coal seam

In comparison to the permeability of the coal seam, the gas permeability coefficient of the coal seam accounts for the viscosity influence of methane flow and is relevant as a measure of the magnitude of CBM flow capacity in coal seams. Monitoring changes in gas pressure within the coal seam is imperative for calculating the gas permeability coefficient. Boreholes K1 and K2 were utilized to meticulously track and evaluate the fluctuations of this parameter. Active pressure measurement was used to monitor the coal seam gas pressure. Following the replenishment of gas pressure in borehole K1 to 0.55 MPa, a substantial amount of water emerged from the borehole, and no gas was observed, leading to the declaration of the borehole as invalid. In this

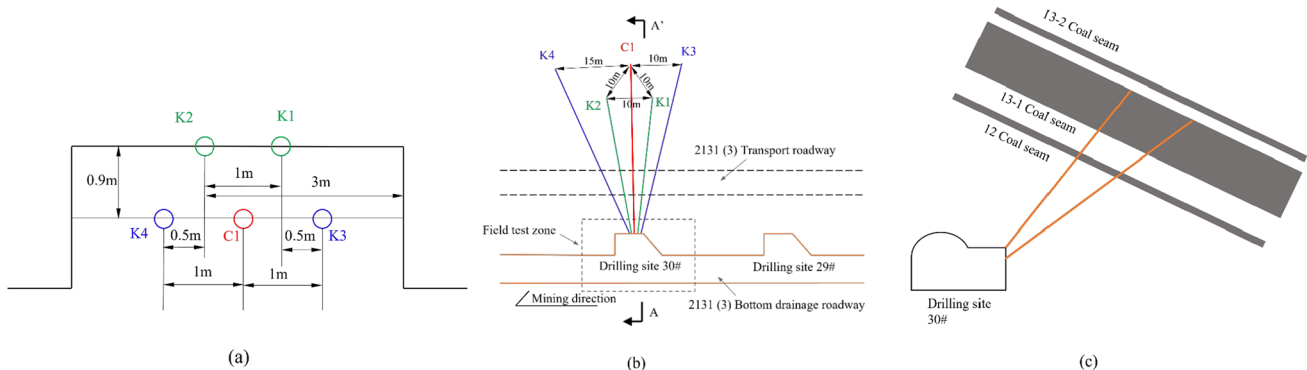


Fig. 12 Field test program **a** Opening position **b** Top view of drilling site 30# **c** A-A' cutaway view

Table 2 Calculated parameters of gas permeability coefficient of C13-1 coal seam

Item	Coal seam gas pressure (MPa)	Atmospheric pressure in the roadway (MPa)	Time (d)	Gas flow rate from boreholes (m ³ /d)	Length of the hole in the coal (m)	Gas content coefficient (MPa ^{0.5})	Gas permeability coefficient (m ² /MPa ² d)
Before antireflection	1.08	0.1	0.77	0.1497	6.1	4.9344	0.0023
After antireflection	1.08	0.1	1.02	0.2735	6.1	4.9344	0.0092

study, the gas permeability coefficient of the coal seam was determined using the radial flow method as the methodology for this research investigation (Administration 2019). The natural gas outflow from the borehole was recorded as the gas pressure stabilised. Table 2 lists the parameters necessary to calculate the coal seam gas permeability coefficient after 1110 min of monitoring. The data in Table 2 clearly indicates an enhancement in the gas permeability coefficient caused by the CSW intervention.

3.4 Inspection of gas extraction

Figure 13 illustrates the variations in the flow rate of pure methane and gas in borehole K3 before and after the implementation of CSW. On the eighth day of hole K3 extraction, CSW was employed. As can be seen from the elliptical area in Fig. 13, the pure methane and gas flowrates exhibit a significant increase on the day of the antireflection operation. The observed phenomenon can be attributed to the conversion of closed pores in the coal into open pores through the combined effects of CSW antireflection and the interconnection of micro-cracks. This process results in the establishment of a well-developed three-dimensional network, facilitating the efficient transport of methane gas within the coal seam. In addition, through repeated exposure to CSW, the adsorbed gas in the coal seam is gradually desorbed, and the desorbed gas flows into a well-developed gas traffic network, contributing to gas extraction. Notably, the increased gas production shown in Fig. 13 demonstrates the usefulness of the CSW technique in enhancing the permeability of the coal seam within at least 10 m of the antireflection hole. This result corroborates the mathematical model of the effective CSW influence range in Sect. 2.

To further validate the correctness of the mathematical model of the effective range of influence for the CSW given in Sect. 2, the variation curves of the pure methane flowrate and gas flowrate for borehole K4 were plotted. Borehole K4 was 15 m from borehole C1, which exceeded the value (10.29 m) obtained using the mathematical model. Figure 14 illustrates the variation in the extraction flowrate from K4. There was no significant reduction or increase in the pure methane or gas flow rate by day 8 (the day of the antireflection operation). We suspect that the trend shown in Fig. 14 is due to the gradual depletion of free gas within the area of influence of borehole K4 as the extraction time increases. Due to the seam's low permeability, the magnitude of negative pressure in drainage proves inadequate for facilitating long-range gas transport. Figure 14 shows a different trend in the curves compared with that shown in Fig. 13. This indicates that the CSW action did not effectively influence hole K4. This result further validates the mathematical model presented in Sect. 2.

Table 3 summarises the data obtained through boreholes K1, K2, K3, and K4 for the data analysis of the CSW antireflection field tests. The gas permeability coefficient for the K1 borehole is unavailable due to the absence of gas pressure measurements for borehole K1.

The changes in some of the parameters in Table 3 are shown visually. After employing CSW antireflection, the gas permeability coefficient of the coal seam showed a threefold increase, as evidenced by the measurements taken at borehole K2. The extraction data from borehole K3 shows an increase in the average pure methane flowrate and average gas flowrate by a factor of 13.72 and 11.48, respectively, after CSW antireflection. Although the CSW

Fig. 13 Pure methane flowrate and gas flowrate variation curves for borehole K3

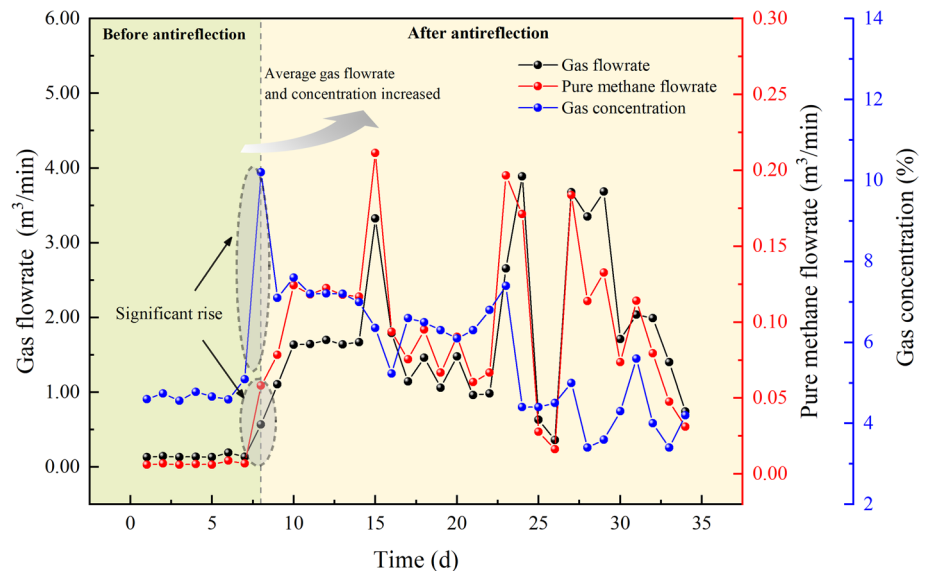


Fig. 14 Pure methane flowrate and gas flowrate variation curves for borehole K4

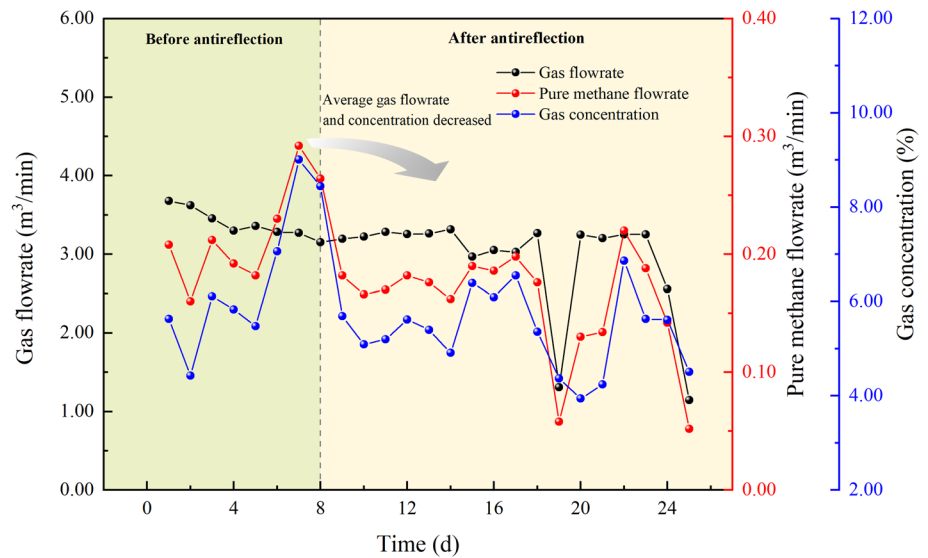


Table 3 Data analysis of CSW field test

Borehole	Distance to anti-reflection hole (m)	Parameters	Increment
K1	5	Gas permeability coefficient of coal seam	–
K2	5	Gas permeability coefficient of coal seam	3 times
K3	10	Average pure methane flowrate	13.72 times
		Average gas flowrate	11.48 times
		Average gas concentration	1.5 times
K4	15	Average pure methane flowrate	– 0.22 times
		Average gas flowrate	– 0.14 times
		Average gas concentration	– 0.11 times

Note: No data were measured in K1 borehole

effective influence radius cannot be precisely determined, the extraction data from boreholes K4 and K3 at least suggest that the mathematical model in Sect. 2 can be used to guide engineering practice.

3.5 Response of borehole cluster gas extraction to CSW

It is well known that dozens of boreholes are typically used as a group to extract CBM. The impact of CSW on CBM extraction from borehole clusters needs to be further investigated. For this reason, drilling site 29# was selected for testing. The 72 boreholes in drilling site 29# had been extracting CBM for 13 days before the test. The distribution of boreholes in drilling site 29# is shown in Fig. 15a. In Fig. 15a only the position of the bottom of the extraction borehole is shown, thus ensuring the simplicity of the schematic. Figure 15b shows the gas extraction pipelines finally being aggregated into one pipeline in which the gas flow and methane concentration are monitored.

Figure 16 shows the changes in gas flow, pure methane flow, and methane concentration before and after antireflection at drilling site 29#. On the day of the CSW antireflection, the gas concentration rose sharply, reaching a maximum peak of 71.2%. Pure methane flowrate rises significantly on the day after CSW antireflection, reaching a maximum peak of 2.59 m³/min after 14 days, and then gradually declines. The most significant change in gas extraction occurred within two days of the CSW antireflection. We observed cumulative gas production and cumulative pure methane production of 2730.61 m³ and 1245.24 m³ respectively, on the day of the antireflection, with an average gas concentration of 51%.

The average gas flowrate, average pure methane flowrate, and average gas concentration all increased after CSW antireflection, and the changes in these data are shown in Table 4.

Figure 17 illustrates the changes in cumulative flow rates of pure methane and gas before and after implementing CSW antireflection. Initially, both the cumulative flow

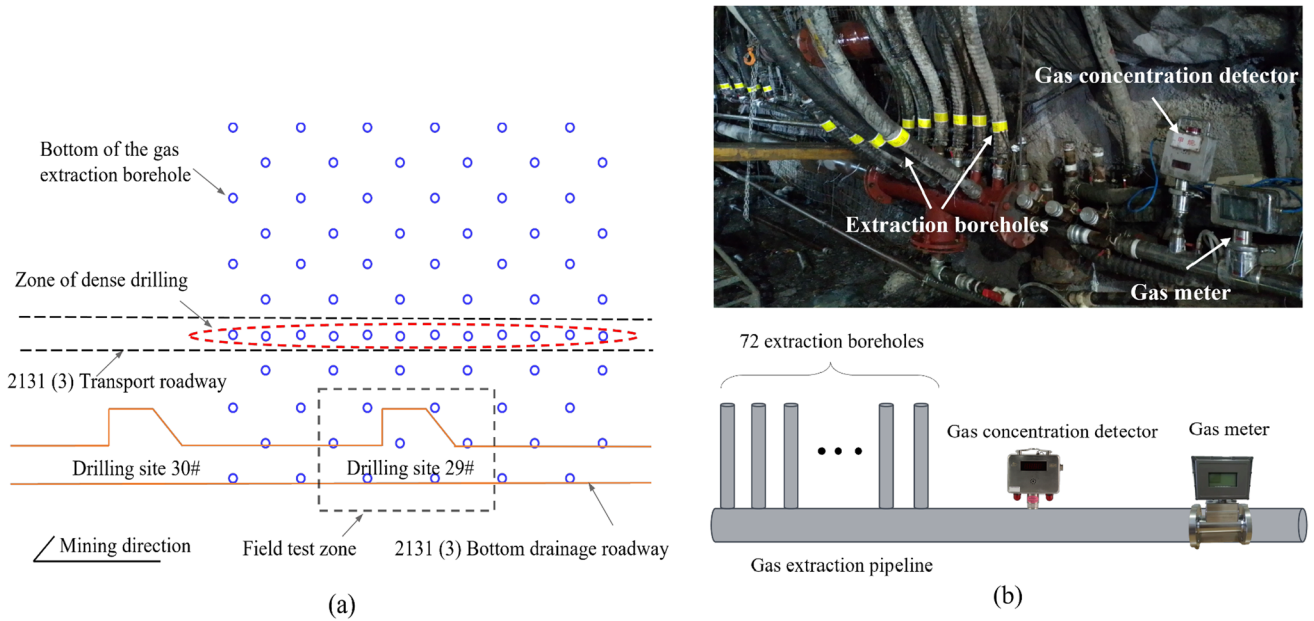


Fig. 15 Testing and monitoring program **a** Location of extraction boreholes in drilling site 29# **b** Diagram of gas monitoring

Fig.16 Gas extraction data from drilling site 29#

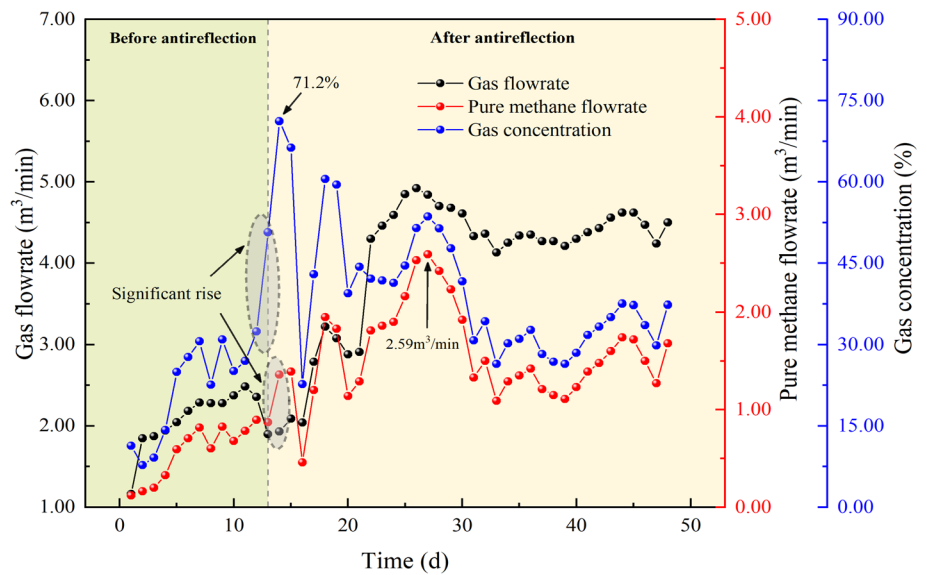


Table 4 Data variation in the gas extraction borehole cluster

Site	Parameters	Before antireflection	After antireflection	Increment
Drilling site 29#	Average pure methane flowrate	0.56 m ³ /min	1.55 m ³ /min	1.78 times
	Average gas flowrate	2.09 m ³ /min	3.98 m ³ /min	0.90 times
	Average gas concentration	21.99%	40.13%	0.83 times

rate of pure methane and gas showed slow growth. However, the growth rate of both increased significantly after the implementation of CSW antireflection. The cumulative flow rates of pure methane and gas were analyzed using

linear regression with the number of extraction days as the independent variable. After implementing CSW antireflection, the fitted line slope for cumulative pure methane flowrate exhibited an increase from 935.058 to 2345.892, while

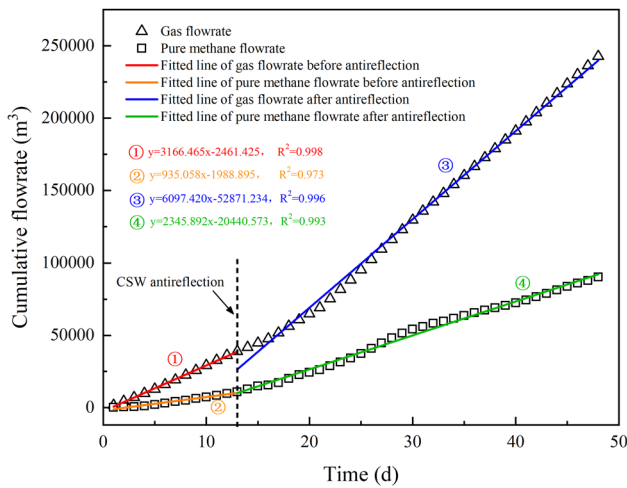


Fig. 17 Evolution of cumulative flowrate

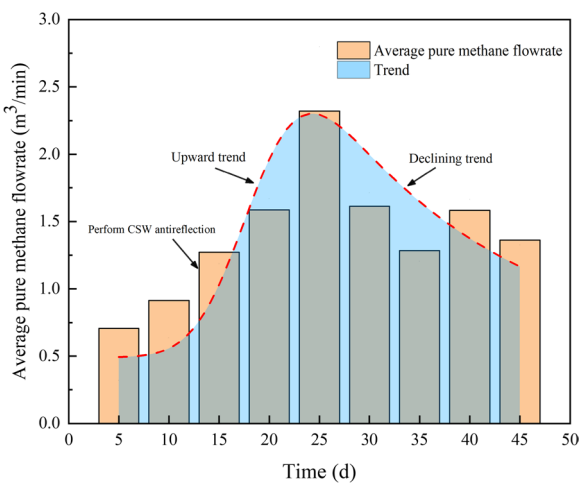


Fig. 18 Variation of the average pure methane flowrate with extraction time

the fitted line slope for cumulative gas flowrate showed an increase from 3166.465 to 6097.420. These findings demonstrate that CSW antireflection has a significant positive impact on CBM production.

During the extraction process, there is a gradual decrease in the gas pressure gradient surrounding the borehole, which results in a corresponding reduction in the gas flow rate within the cluster of extraction boreholes. Figure 18 showcases the computation of the average flow rate of pure methane over a five-day interval, providing a visualization of the temporal changes. The average flow rate of pure methane increases and then gradually decreases, indicating that gas extraction takes some time to reach its optimum state after CSW antireflection. After 36 days of CSW antireflection, the average methane flowrate was still 2.11 times greater than before CSW

antireflection. The study demonstrates that efficient extraction continues for at least 36 days after CSW antireflection on soft and low-permeability coal seams.

4 Discussion

4.1 Advantages of CSW in water conservation

A shared characteristic inherent in both hydraulic fracturing and CSW techniques is the requisite use of water throughout the operational process. Hydraulic fracturing is controversial because of its environmental unfriendliness and water wastage (Sampath et al. 2019; Scanlon et al. 2014). In comparison, CSW produces no environmental pollutants in the antireflection process and requires very little water. In addition, the CSW achieves higher energy transfer efficiency under water bath operating conditions. This means that the CSW is more energy efficient. The determination of water injection volume during the hydraulic fracturing of coal seams adheres to the following formula (Wang 2019):

$$V = V_w + V_b \tag{24}$$

$$V_w = V_c k \tag{25}$$

$$V_d = \pi r_b^2 l_b + \pi r_p^2 l_p \tag{26}$$

where V_w represents the water consumption of the coal seam affected by hydraulic fracturing, k is the porosity of the coal, V_c is the volume of the coal seam affected by hydraulic fracturing, and V_d is the volume of water used to fill water pipes and hydraulic fracturing boreholes. Additionally, r_b , r_p , l_b , and l_p denote the radius of the borehole, the radius of the pipe, the length of the borehole, and the length of the water pipe, respectively.

In this study, the permeability of the C13-1 seam is recorded as 3.36%. The radius of the CSW antireflection is approximately 10 m, and the average thickness of the coal seam is 5.9 m. Consequently, the volume of the coal seam with CSW antireflection is estimated at 1853.6 m³. When hydraulic fracturing is employed in borehole C1 to antireflect an equivalent volume of coal seam without considering the length of the pipe, V_w , V_d , and V can be calculated from the data in Table 1 as 62.3, 0.7, and 63.0 m³, respectively. Notably, during CSW, it suffices to ensure that the borehole is filled with water, resulting in a water consumption of 0.7 m³. Remarkably, with an equivalent volume of anti-reflective coal seam, hydraulic fracturing consumes 90 times more water than CSW.

4.2 The effective CSW influence range

Previous CSW research has primarily focused on laboratory experiments, resulting in numerous valuable conclusions. However, there is a lack of field tests, especially concerning soft and low-permeability coal seams. The Huainan coalfield, recognized as a highly significant coal-producing region in China, contains a predominant majority of soft and low-permeability coal seams. Performing field trials to enhance CBM production using the CSW method in the Huainan coalfield is a valuable endeavor that addresses the low CBM production in this geological context. It holds significant importance for both coal mine safety and environmental protection.

This study implemented CSW technology in the treatment of soft and low-permeability coal seams through field applications and introduced a novel mathematical model for CSW antireflection. Notably, this research represents the inaugural instance of such investigations. Significantly, the study opted for the planar stress wave theory over the conventional one-dimensional stress wave theory typically employed in coal seam fracturing reports. This decision enhances the accuracy and precision of the mathematical model. The amalgamation of calculations from the mathematical model and results from field tests demonstrated that CSW can effectively improve CBM extraction within a range of approximately 10 m. Nevertheless, prior studies have indicated that CSW-enhanced CBM extraction can

extend beyond the 10-m range (An et al. 2020; Zhang et al. 2019). Table 5 provides a summary of the effective CSW influence ranges measured in prior field tests.

The consistent coefficient of the test site coals in Table 5 are greater than for the coal covered in this paper. The soft nature of the coal in this paper may be responsible for the smaller radius of influence. Specifically, a coal seam with small consistent coefficient will have a larger crushed zone, which means that a large amount of energy is consumed in the crushed zone (Tao et al. 2020). Furthermore, the energy-absorbing nature of soft coal compared to hard coal leads to faster dissipation of stress waves. The looser structure of soft coal also hinders effective pore improvement. In addition, the energy magnitude of the EM is an important factor in the effective CSW influence range. Past studies have shown that the magnitude of EM energy is highly correlated with changes in coal pore structure (Li 2015; Shi et al. 2016).

4.3 Impact of CSW on the borehole cluster

Gas extraction borehole clusters serve as the smallest unit for CBM extraction. The impact of CSW on the gas extraction borehole cluster becomes apparent through changes in gas flowrate, concentration, and cumulative production. This underscores the practical significance of CSW in engineering applications for soft and low-permeability coal seams. In the Huainan coalfield, both the 11–2 coal seam and the C13-1 coal seam exhibit characteristics of being soft and low-permeability coal seams, sharing similar gas geological conditions. A field trial of hydraulic fracturing against the 11–2 coal seam was conducted by Cai and Liu (2016) at Guqiao coal mine in Huainan. As shown in Fig. 19, the hydraulic fracturing and gas extraction drill holes were arranged similarly to the 29# drilling site (Cai and Liu 2016).

Table 5 The effective CSW influence range

Reference	An (2020)	Su (2020)	Wang (2019)	Zhang (2019)
Radius of influence	30 m	17 m	17 m	15 m

Fig. 19 Layout of boreholes (Cai and Liu 2016) **a** Layout of antireflection borehole **b** Location of extraction and antireflection boreholes

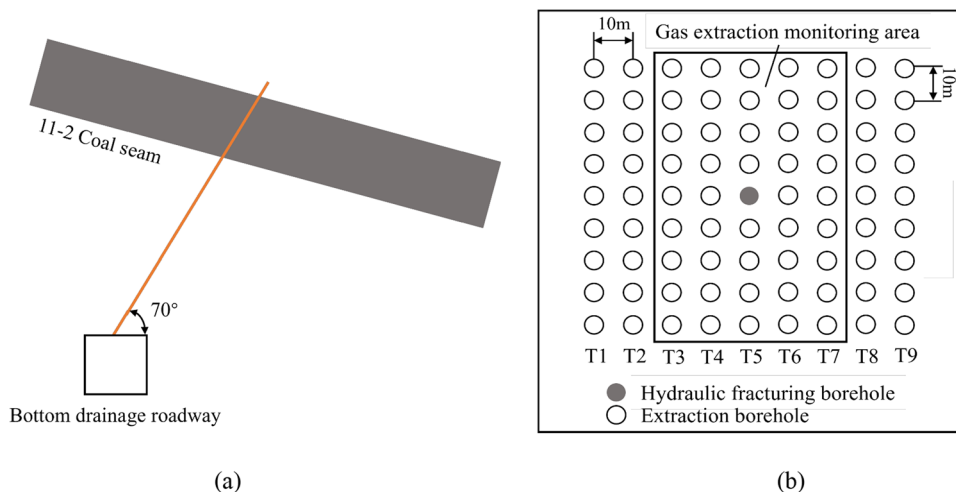


Figure 20 displays the variation in single-hole pure methane flowrate over time following CSW treatment and hydraulic fracturing. Before anti-reflective measures, the single-hole pure methane flow rates in the 11–2 and C13-1 coal seams were $0.003 \text{ m}^3/\text{min}$ and $0.0078 \text{ m}^3/\text{min}$, respectively. Overall, the single-hole pure methane flowrate after CSW is greater, compared to the single-hole pure methane flowrate after hydraulic fracturing. On average, CSW and hydraulic fracturing can increase the pure methane flow rate of a single hole by 1.88 times and 1.38 times, respectively. Consequently, this underscores significant potential for enhanced gas extraction using CSW within a cluster of boreholes situated in soft and low-permeability coal seams.

It should be emphasized that in the context of the CSW anti-reflection process, EM detonations occur multiple times, whereas the mathematical model presented in Sect. 2 is founded upon a single detonation of EM. However, this does not invalidate the effective CSW influence range as repeated blasts of explosives primarily impact the blast crush and fracture zones rather than the vibration zone (Wang et al. 2021a, b). The effective CSW influence range, determined based on PPV, is confined to the vibration zone. Numerical simulations as a useful tool can be employed to investigate the dynamic response characteristics of coal seams under multiple blasting loads from EM. Some commercial software such as ANSYS/LS-DYNA have been widely utilized to calculate the dynamic response of rocks under dynamic loading (Yi et al. 2017, 2018). It is a potential approach to further explore the impact of CSW on enhancing CBM in soft and low-permeability coal seams.

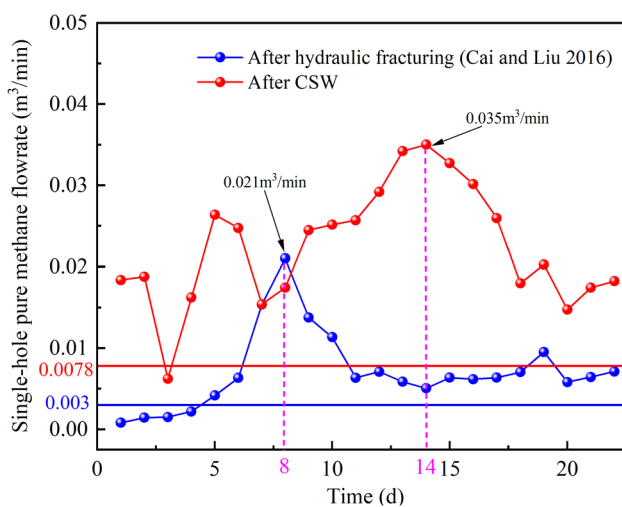


Fig. 20 Average pure methane flow rate for single-hole

5 Conclusions

The CSW technology is a new and promising technique for enhanced CBM extraction. In this study, CSW was used for antireflection in soft and low-permeability coal seams. A mathematical model of the dynamic response of the coal seam was established based on explosion mechanics, rock dynamics, and elasticity. The effective influence range of CSW was calculated for the physical parameters of coal seams in the Xieqiao coal mine. The calculation results were used to design a field-test program for CSW antireflection. The primary findings derived from this investigation are outlined below:

- (1) The governing equations for CSW-generated stress waves in coal are given, and a comprehensive inversion of the dynamic response state of coal is carried out by the Laplace transform. Combined with the coal damage criterion, the extent of the CSW-induced crushed and fracture zones was deduced to be 0.424 m and 1.455 m, respectively. Furthermore, a mathematical model of the effective CSW influence range was developed using the PPV decay law as the basis.
- (2) The radius $R_3 = 10.29 \text{ m}$ of the effective range of influence for CSW was calculated using the mathematical model at the C13-1 coal seam project site in the Xieqiao Mine. The results of the extraction flow rate comparison between holes K3 and K4 further validated the reliability of the mathematical model. This will serve as a guide for engineering CSW anti-reflection holes in similar geological conditions.
- (3) The field test data indicate that CSW significantly enhances CBM extraction within the effective range of influence of CSW. The application of CSW in a cluster of gas extraction boreholes resulted in a maximum gas concentration of 72% and an increase in the average pure methane flow rate of 1.78 times, allowing for at least 36 days of efficient gas extraction. Field tests proved that the CSW technology is promising for enhancing CBM, in soft and low-permeability coal seams.

Acknowledgements This work was supported by the National Natural Science Foundation of China (52074013, 52374179), China Huaneng Group Science and Technology Project (HNKJ20-H87), Natural Science Foundation of Anhui Province (2208085ME125), and Hefei Comprehensive National Science Center (21KZS216), which are gratefully appreciated. Thanks to the workers and engineers involved in the field tests.

Author contributions Guodong Qiao: Conceptualization, Methodology, Investigation, Writing—original draft, Visualization. Zegong Liu: Resources, Supervision, Funding acquisition. Yongmin Zhang: Project

administration. Changping Yi: Methodology, Investigation. Kui Gao: Formal analysis. Shigui Fu: Data curation, Investigation. Youzhi Zhao: Validation.

Declarations

Competing interest The authors declare that they have no known competing financial interests or personal relationships that could have appeared to influence the work reported in this paper.

Open Access This article is licensed under a Creative Commons Attribution 4.0 International License, which permits use, sharing, adaptation, distribution and reproduction in any medium or format, as long as you give appropriate credit to the original author(s) and the source, provide a link to the Creative Commons licence, and indicate if changes were made. The images or other third party material in this article are included in the article's Creative Commons licence, unless indicated otherwise in a credit line to the material. If material is not included in the article's Creative Commons licence and your intended use is not permitted by statutory regulation or exceeds the permitted use, you will need to obtain permission directly from the copyright holder. To view a copy of this licence, visit <http://creativecommons.org/licenses/by/4.0/>.

References

- Aici Q, Yongmin Z, Bin K (2012) Application of high power pulse technology in unconventional gas development. In: Proceeding of 2nd CAE/NEA energy forum. Coal Industry Press, Beijing 1112–1115
- Shigang AN, Dianfu CH, Yongmin ZH, Delei KO, Yang LI, Di ZH, Yang WA (2020) Application of controllable electric pulse wave permeability-enhancing technology in the low-permeability coal seams. *Coal Geol Explor* 48(4):21. <https://doi.org/10.3969/j.issn.1001-1986.2020.04.020>
- Bauer A, Calder P (1978) Open pit and blasting seminar. Dissertation, Queens University, Kingston
- Busch A, Gensterblum Y (2011) CBM and CO₂-ECBM related sorption processes in coal: a review. *Int J Coal Geol* 87(2):49–71. <https://doi.org/10.1016/j.coal.2011.04.011>
- Cai F, Liu Z (2016) Simulation and experimental research on upward cross-seams hydraulic fracturing in deep and low-permeability coal seam. *J China Coal Soc* 41(01):113–119. <https://doi.org/10.13225/j.cnki.jccs.2015.9014>
- Cho SH, Miyake H, Kimura T, Kaneko K (2003) Effect of the waveform of applied pressure on rock fracture process in one free-face model. *Sci Technol Energetic Mater*. <https://doi.org/10.1128/AEM.72.4.2359-2365.2006>
- Cho SH, Cheong SS, Yokota M, Kaneko K (2016) The dynamic fracture process in rocks under high-voltage pulse fragmentation. *Rock Mech Rock Eng* 49(10):3841–3853. <https://doi.org/10.1007/s00603-016-1031-z>
- Cohen AM (2007) Numerical methods for Laplace transform inversion. Springer Science and Business Media, New York
- Dai J (2001) Calculation of radii of the broken and cracked areas in rock by a long charge explosion. *J Liaoning Tech Univ Nat Sci* 20(2):144–147. <https://doi.org/10.3969/j.issn.1008-0562.2001.02.005>
- Dubner H, Abate J (1968) Numerical inversion of Laplace transforms by relating them to the finite Fourier cosine transform. *J ACM* 15(1):115–123. <https://doi.org/10.1145/321439.321446>
- Durbin F (1974) Numerical inversion of Laplace transforms: an efficient improvement to Dubner and Abate's method. *Comput J* 17(4):371–376. <https://doi.org/10.1093/comjnl/17.4.371>
- Duvall WI (1953) Strain-wave shapes in rock near explosions. *Geophysics* 18(2):310–323. <https://doi.org/10.1190/1.1437875>
- Esen S, Onederra I, Bilgin HA (2003) Modelling the size of the crushed zone around a blasthole. *Int J Rock Mech Min Sci* 40(4):485–495. [https://doi.org/10.1016/S1365-1609\(03\)00018-2](https://doi.org/10.1016/S1365-1609(03)00018-2)
- Fan Y, Miao X, Gao Q, Leng Z, Zheng J, Wu J (2022) Influence of water depth on the range of crushed zones and cracked zones for underwater rock drilling and blasting. *Int J Geomech* 22(10):04022164. [https://doi.org/10.1061/\(ASCE\)GM.1943-5622.000248](https://doi.org/10.1061/(ASCE)GM.1943-5622.000248)
- Grinenko A, Sayapin A, Gurovich VT, Efimov S, Felsteiner J, Krasik YE (2005) Underwater electrical explosion of a Cu wire. *J Appl Phys* 97(2):023303. <https://doi.org/10.1063/1.1835562>
- Han R, Zhou H, Liu Q, Wu J, Jing Y, Chao Y et al (2015) Generation of electrohydraulic shock waves by plasma-ignited energetic materials: I. Fundamental mechanisms and processes. *IEEE Trans Plasma Sci* 43(12):3999–4008. <https://doi.org/10.1109/TPS.2015.2468064>
- Hu Y, Shi H, Li T, Tao Z, Li X, Wu J et al (2022) Underwater shock wave generated by exploding wire ignited energetic materials and its applications in reservoir stimulation. *IEEE Trans Plasma Sci* 50(9):2520–2527. <https://doi.org/10.1109/TPS.2022.3175485>
- Hustrulid W, Lu W (2002) Some general design concepts regarding the control of blast-induced damage during rock slope excavation. In: Proceedings of the 7th international symposium on rock fragmentation by blasting. Beijing, China 595–604
- Jackson DD, Anderson DL (1970) Physical mechanisms of seismic-wave attenuation. *Rev Geophys* 8(1):1–63. <https://doi.org/10.1029/RG008i001p00001>
- Jin X (2013) The generation and attenuation mechanism of blasting induced seismic wave. Dissertation, Wuhan University, Wuhan
- Johnston DH, Toksoz M, Timur A (1979) Attenuation of seismic waves in dry and saturated rocks II. Mechanisms. *Geophysics* 44(4):691–711. <https://doi.org/10.1190/1.1440970>
- Kristiansen M, Hatfield LL, Lojewski D (1998) High voltage water breakdown studies. Defense Special Weapons Agency, Alexandria, VA
- Li H (2015) Behavior and mechanism of fracturing and enhanced-permeability of coals with electric pulse stress waves. Dissertation, China University of Mining and Technology, Xuzhou
- Li H, Qi Y, Zhou X, Zhang Y, Chen Y (2021) Development characteristics of coal microfracture and coal petrology control under cyclic high voltage electrical pulse. *Coal Geol Explor* 49(04):105–113. <https://doi.org/10.3969/j.issn.1001-1986.2021.04.013>
- Lin B, Zhang X (2022) Technology and research progress of plasma induced coal and rock cracking and antireflection. *Min Saf Environ Prot* 49(4):12–21. <https://doi.org/10.19835/j.issn.1008-4495.2022.04.002>
- Li L, Zhang H, Pan Y, Ju X, Tang L, Li M (2022) Influence of stress wave-induced disturbance on ultra-low friction in broken blocks. *Int J Coal Sci Technol* 9(1):22. <https://doi.org/10.1007/s40789-022-00490-4>
- Liu Q, Yao W, Zhang Y, Wang Y, Tang J, Zhao Z et al (2019) Study on ignition mechanism and shockwave characteristics of nitramine powders ignited by microsecond exploding wire plasma. *IEEE Trans Plasma Sci* 47(10):4500–4505. <https://doi.org/10.1109/TPS.2019.2921668>
- Liu Q, Ding W, Han R, Wu J, Jing Y, Zhang Y et al (2017) Fracturing effect of electrohydraulic shock waves generated by plasma-ignited energetic materials explosion. *IEEE Trans Plasma Sci* 45(3):423–431. <https://doi.org/10.1109/TPS.2017.2659761>
- Liu T, Lin B, Fu X, Gao Y, Kong J, Zhao Y et al (2020) Experimental study on gas diffusion dynamics in fractured coal: a better

- understanding of gas migration in in-situ coal seam. *Energy* 195:117005. <https://doi.org/10.1016/j.energy.2020.117005>
- Lu W, Leng Z, Chen M, Yan P, Hu Y (2016) A modified model to calculate the size of the crushed zone around a blast-hole. *J South Afr Inst Min Metall* 116(5):412–422. <https://doi.org/10.17159/2411-9717/2016/v116n5a7>
- Ma GW, An XM (2008) Numerical simulation of blasting-induced rock fractures. *Int J Rock Mech Min Sci* 45(6):966–975. <https://doi.org/10.1016/j.ijrmms.2007.12.002>
- Meng Y, Liu S, Li Z (2018) Experimental study on sorption induced strain and permeability evolutions and their implications in the anthracite coalbed methane production. *J Pet Sci Eng* 164:515–522. <https://doi.org/10.1016/j.petrol.2018.01.014>
- Miklowitz J (1978) *The theory of elastic waves and waveguides*. North Holland Publishing Company, California
- National mine safety administration (2019) Measuring method for gas permeability coefficient of coal seam—radial flow method. MT/T 1173–2019 Beijing. https://www.chinamine-safety.gov.cn/zfxxgk/fdzdgnr/zcfg/hybz_01/mkanj/index_1.shtml
- Qin L, Zhai C, Liu S, Xu J (2018) Mechanical behavior and fracture spatial propagation of coal injected with liquid nitrogen under triaxial stress applied for coalbed methane recovery. *Eng Geol* 233:1–10. <https://doi.org/10.1016/j.enggeo.2017.11.019>
- Rossmannith H, Uenishi K, Kouzniak N (1997) Blast wave propagation in rock mass—part I: monolithic medium. *Fragblast* 1(3):317–359. <https://doi.org/10.1080/13855149709408402>
- Sampath KHS, Perera MSA, Elsworth D, Ranjith PG, Matthai SK, Rathnaweera T et al (2019) Effect of coal maturity on CO₂-based hydraulic fracturing process in coal seam gas reservoirs. *Fuel* 236:179–189. <https://doi.org/10.1016/j.fuel.2018.08.150>
- Sandoval DR, Yan W, Michelsen ML, Stenby EH (2018) Influence of adsorption and capillary pressure on phase equilibria inside shale reservoirs. *Energy Fuels* 32(3):2819–2833. <https://doi.org/10.1021/acs.energyfuels.7b03274>
- Scanlon BR, Reedy RC, Nicot JP (2014) Comparison of water use for hydraulic fracturing for unconventional oil and gas versus conventional oil. *Environ Sci Technol* 48(20):12386–12393. <https://doi.org/10.1021/es502506v>
- Shao X (2014) Research of fracture law and deep hole advance blasting technology in hard and thick sandstone roof. Dissertation, Anhui University of Science and Technology, Huainan
- Sharpe JA (1942) The production of elastic waves by explosion pressures I. Theory and empirical field observations. *Geophysics* 7(2):144–154. <https://doi.org/10.1190/1.1445002>
- Shi H, Hu Y, Li T, Tao Z, Li X, Wu J et al (2021) Detonation of a nitromethane-based energetic mixture driven by electrical wire explosion. *J Phys D Appl Phys* 55(5):05LT01. <https://doi.org/10.1088/1361-6463/ac3174>
- Shi Q, Qin Y, Li H, Qiu A, Zhang Y, Zhou X et al (2016) Response of pores in coal to repeated strong impulse waves. *J Nat Gas Sci Eng* 34:298–304. <https://doi.org/10.1016/j.jngse.2016.06.067>
- Si L, Li Z, Yang Y, Gao R (2019) The stage evolution characteristics of gas transport during mine gas extraction: its application in borehole layout for improving gas production. *Fuel* 241:164–175. <https://doi.org/10.1016/j.fuel.2018.12.038>
- Su S (2020) Application of controllable shock wave for permeability enhancement in hard thick coal seam. *Coal Eng* 52(09):71–75
- Sun R, Ji Y, Lin L, Hu A, Wu R, Chen D (2015) On the effect of ultrasonic stimulation on the desorption of coalbed methane. *J EXP Mech* 30(01):94–100. <https://doi.org/10.7520/1001-4888-14-056>
- Sun X (1987) *Material mechanics*. People's Education Press, Beijing
- State administration for market regulation (2014) Safety regulations for blasting. GB 6722–2014 Beijing. <https://openstd.samr.gov.cn/bzgk/gb/newGbInfo?hcno=B5C47C47122DC805A42E0244B43365C1>
- Tang Z, Yang S, Xu G, Sharifzadeh M, Zhai C (2018) Investigation of the effect of low-temperature oxidation on extraction efficiency and capacity of coalbed methane. *Process Saf Environ Prot* 117:573–581. <https://doi.org/10.1016/j.psep.2018.06.006>
- Tao J, Yang X-G, Li H-T, Zhou J-W, Fan G, Lu G-D (2020) Effects of in-situ stresses on dynamic rock responses under blast loading. *Mech Mater* 145:103374. <https://doi.org/10.1016/j.mechmat.2020.103374>
- Taylor MJ (2002) Plasma propellant interactions in an electrothermal-chemical gun. Dissertation, Cranfield University, Cranfield Village
- Trivino L, Mohanty B, Munjiza A (2009) Seismic radiation patterns from cylindrical explosive charges by analytical and combined finite-discrete element methods. In: Proceedings of the 9th international symposium on rock fragmentation by blasting, Fragblast 9: 415–426.
- Tu Q, Cheng Y, Guo P, Jiang J, Wang L, Zhang R (2016) Experimental study of coal and gas outbursts related to gas-enriched areas. *Rock Mech Rock Eng* 49(9):3769–3781. <https://doi.org/10.1007/s00603-016-0980-6>
- Wang H, Wang Z, Wang J, Wang S, Wang H, Yin Y et al (2021a) Effect of confining pressure on damage accumulation of rock under repeated blast loading. *Int J Impact Eng* 156:103961. <https://doi.org/10.1016/j.ijimpeng.2021.103961>
- Wang Q (2019) Experimental study on stratified section hydraulic fracturing gas anti-reflection of 8006 working face in Wuyang mine. *Coal Chem Ind* 42(10):102–105. <https://doi.org/10.19286/j.cnki.cci.2019.10.028>
- Wang W (1984) *Hole blasting*. China Coal Industry Publishing House, Beijing
- Wang X, Li W (2019) Analysis of the application of controlled shock wave penetration enhancement technology in Jining coal mine. *Shanxi Coking Coal Sci Technol* 43(02):4–7
- Wang Z, Wang H, Wang J, Tian N (2021b) Finite element analyses of constitutive models performance in the simulation of blast-induced rock cracks. *Comput Geotech* 135:104172. <https://doi.org/10.1016/j.compgeo.2021.104172>
- Wang K, Zhang G, Wang Y, Zhang X, Li K, Guo W, Du F (2022) A numerical investigation of hydraulic fracturing on coal seam permeability based on PFC-COMSOL coupling method. *Int J Coal Sci Technol* 9(1):10. <https://doi.org/10.1007/s40789-022-00484-2>
- Wu S, Tang D, Li S, Chen H, Wu H (2016) Coalbed methane adsorption behavior and its energy variation features under supercritical pressure and temperature conditions. *J Pet Sci Eng* 146:726–734. <https://doi.org/10.1016/j.petrol.2016.07.028>
- Xie LX, Lu WB, Zhang Q, Jiang Q, Chen M, Zhao J (2017) Analysis of damage mechanisms and optimization of cut blasting design under high in-situ stresses. *Tunn Undergr Sp Technol* 66:19–33. <https://doi.org/10.1016/j.tust.2017.03.009>
- Xu J, Zhai C, Liu S, Qin L, Sun Y (2017) Feasibility investigation of cryogenic effect from liquid carbon dioxide multi cycle fracturing technology in coalbed methane recovery. *Fuel* 206:371–380. <https://doi.org/10.1016/j.fuel.2017.05.096>
- Yan F, Lin B, Zhu C, Shen C, Zou Q, Guo C et al (2015) A novel ECBM extraction technology based on the integration of hydraulic slotting and hydraulic fracturing. *J Nat Gas Sci Eng* 22:571–579. <https://doi.org/10.1016/j.jngse.2015.01.008>
- Yi C, Sjöberg J, Johansson D (2017) Numerical modelling for blast-induced fragmentation in sublevel caving mines. *Tunn Undergr Sp Technol* 68:167–173. <https://doi.org/10.1016/j.tust.2017.05.030>
- Yi C, Johansson D, Greberg J (2018) Effects of in-situ stresses on the fracturing of rock by blasting. *Comput Geotech* 104:321–330. <https://doi.org/10.1016/j.compgeo.2017.12.004>

- Yuan L (2016) Strategic thinking of simultaneous exploitation of coal and gas in deep mining. *J China Coal Soc* 41(01):1–6. <https://doi.org/10.13225/j.cnki.jccs.2015.9027>
- Yuwen H (2006) Numerical simulation and theory study of blasthole fracture controlled blasting with two decoupling interaction charge. Dissertation, Taiyuan University of Technology, Taiyuan
- Zhang Y, Qiu A, Zhou H, Liu Q, Tang J, Liu M (2016) Research progress in electrical explosion shockwave technology for developing fossil energy. *High Voltage Eng* 42(4):1009–1017. <https://doi.org/10.13336/j.1003-6520.hve.20160405010>
- Zhang Y, An S, Chen D, Shi Q, Zhang Z, Zhao Y et al (2019) Preliminary tests of coal reservoir permeability enhancement by controllable shock waves in baode coal mine 8# coal seam. *Saf Coal Mines* 50(10):14–17. <https://doi.org/10.13347/j.cnki.mkaq.2019.10.004>
- Zhao J (2021) Geological constraints and improved models of coal seam reconstruction with controllable shock wave. Dissertation, China University of Mining and Technology, Xuzhou
- Zhou H, Han R, Liu Q, Jing Y, Wu J, Zhang Y et al (2015a) Generation of electrohydraulic shock waves by plasma-ignited energetic materials: II. Influence of wire configuration and stored energy. *IEEE Trans Plasma Sci* 43(12):4009–4016. <https://doi.org/10.1109/TPS.2015.2469593>
- Zhou H, Zhang Y, Li H, Han R, Jing Y, Liu Q et al (2015b) Generation of electrohydraulic shock waves by plasma-ignited energetic materials: III. Shock wave characteristics with three discharge loads. *IEEE Trans Plasma Sci* 43(12):4017–4023. <https://doi.org/10.1109/TPS.2015.2477357>
- Zhu F, Liu Z, Zuo Y, Yang N, Huang A-C (2023) Damage and failure characteristics of coal and surrounding rock under shaped blasting. *Process Saf Environ Prot* 176:56–64. <https://doi.org/10.1016/j.psep.2023.06.014>
- Zong Q, Tian L, Wang H (2012) Study and application on rock damage range by blasting with water-decoupled charge. *Blasting* 29(02):42–46. <https://doi.org/10.3963/j.issn.1001-487X.2012.02.011>

Publisher's Note Springer Nature remains neutral with regard to jurisdictional claims in published maps and institutional affiliations.